JOURNAL OF AIRCRAFT
Vol. 48, No. 4, July–August 2011

Simulating the Flows About Cargo Containers Used During Parachute Airdrop Operations

Mark McQuilling* and Jean Potvin†
Saint Louis University, St. Louis, Missouri 63103
and
Justin Riley‡
Natick Soldier Research, Development, and Engineering Center, Natick, Massachusetts 01760

DOI: 10.2514/1.C031299

This paper presents results from a Navier–Stokes finite volume flow solver simulating the flowfields around a platform and cargo configuration representative of platforms used for military parachute airdrops. The platform and cargo configuration consists of a flat-plate model with an aspect ratio (width/length) of 0.56 outfitted with a nose bumper, upon which a box representing cargo is placed. This combination is simulated in conditions approximating the fall of a container before and after parachute deployment and inflation, including a full 360° angle-of-attack range at Reynolds numbers of 2.94×10^6 and 9.80×10^6 (freestream velocities of 30 and 100 ft/s). The static simulations approximate those cases in which the tumbling and swinging of the container (mostly before parachute deployment or during descent) is slow enough to approximate near-steady-state flow conditions. Results include lift, drag, and moment coefficients over the range of flow conditions, as well as pressure contours to help elucidate relevant flow physics around the pallet-cargo configuration. Results show the flow orientation (into the nose bumper or flat side first) significantly affects the drag behavior, but not the lift or moment coefficients. Lift-curve slopes match well with previously published data on pallet and cargo geometries as well as flat plates with similar aspect ratios. Drag coefficients were significantly different between flow orientations and also exhibited asymmetry between positive and negative angles of attack.

Nomenclature

C_D	=	drag coefficient
C_L	=	lift coefficient
$C_{L\alpha}$	=	lift-curve slope
C_M	=	moment coefficient
C_p	=	pressure coefficient
q_∞	=	freestream dynamic pressure
Re	=	Reynolds number
R^2	=	coefficient of linear correlation
S	=	model planform area (pallet width × length)
α	=	angle of attack

Introduction

THE main goal of military airdrops is the accurate delivery of cargo via parachute, as dropped from a moving air vehicle [1]. Although computational fluid dynamics (CFD)-based techniques are now routinely being used to analyze the flow about (inflated) parachute canopies, very little has been done in the area of payload container aerodynamics, either simulated in isolation [2–4] or with the platform rigging and canopy overhead [5,6]. This state of affairs is made more complicated by the fact that there are many different dynamic regimes characterizing the flows about parachute payloads during a typical airdrop operation [3,7,8], i.e., during ramp rollout and tipover, free fall before and during parachute deployment, and descent and landing under a fully inflated canopy. To complicate matters even more, the very motions of these payloads are often such that the flows are unsteady and therefore quite specific to the details of the motions themselves. These make first-principle simulations of payload fall and airstream tracking not only very difficult to carry out even on the fastest of computers, but also almost impossible to validate with experimental data. Detailed flow simulations about payloads are usually not necessary for the purpose of parachute peak-load calculation (during the inflation stage) or for container shock-absorption determination (during landing), typically the two most important structural engineering mileposts. But payload flows studies are crucial to the understanding of the containers' motions along the entire trajectory: namely, tumbling motions occurring during ramp tipover and then free fall before parachute deployment and swinging motion during descent under parachute. Understanding the dynamics of tumbling during launch and free fall is bound to become important given that most major parachute malfunctions can be traced back to the initial tangling of the parachute's rigging (i.e., straps and risers) with the corners or other portions of the payload. On the other hand, understanding the dynamics of swinging during descent is particularly important during landing, as horizontal translation during ground impact can lead to load tipover.

As with many other complex phenomena, the understanding of payload aerodynamics begins with detailed CFD-based simulations in the steady regime in order to characterize at least those cases in which the aerodynamics can be approximated as near steady state. Airdropped payload examples representative of this category would include the all-important type-V platforms (normally 108 in. width by 192 in. length by 34 in. height) carrying containers weighing in excess of 10,000 lb, undergoing slow tumbling rates under 1 rad/s in airstreams of 200–300 ft/s. Being in a near-steady flow regime allows the calculation, from the detailed flow simulations, of the payload aerodynamic coefficients C_D, C_L, and C_M, which in turn can be used in six-degree-of-freedom simulations of the fall and tumbling of the container, parachute, and other relevant hardware. Such an approach has been used over the past eight years via the use of the Decelerator System Simulation Application (DSSA) computer

Presented as Paper 2010-4565 at the 28th AIAA Applied Aerodynamics Conference, Chicago, IL, 28 June–1 2010; received 6 November 2010; revision received 14 April 2011; accepted for publication 14 April 2011.

*Assistant Professor, Center for Fluids at All Scales, Department of Aerospace and Mechanical Engineering, 3450 Lindell Boulevard. Member AIAA.

†Professor, Center for Fluids at All Scales, Department of Physics, 3450 Lindell Boulevard. Associate Fellow AIAA.

‡Research Aerospace Engineer, Airdrop Technology Team, 15 Kansas Street. Member AIAA

program [2–4,9]. DSSA is designed to simulate the entire fall dynamics of platforms: containers dropped from the ramps of cargo aircraft, from rollout, to parachute deployment and inflation, to steady descent. It is currently based upon the coupling of an Excel spreadsheet to FORTRAN macros. This computer program was initially developed by NASA to support the recovery of the space shuttle solid rocket boosters [10]. It was extended later to simulate the boilerplate platform drops of the X-38 program [11] and extended again into its current spreadsheet form, under a U.S. Army —NASA partnership, with the latter effort aimed at improving user-friendliness, as well as further developing the program to handle the cargo parachutes and aircraft ramps that are used by the U.S. military. As discussed in [3], the various trajectory outputs of DSSA applying to a typical U.S. Army LVAD (low-velocity airdrop delivery) payload [1] have been compared with actual flight data and found to be in good agreement.

DSSA involves a large number of input parameters, including pallet-container dimensions and weight, extraction and main parachute dimensions and weight, riser and bridle dimensions, and even some specifics of the load-transfer hardware. Crucial input parameters also include those platform-container aerodynamic coefficients previously mentioned, as functions of container pitch angle (i.e., pitch of the long dimension of the container about the axis running along the container's width; pitch angle measured with respect to the horizontal). Such coefficients are computed separately from DSSA, i.e., via the use of CFD. In its current implementation, DSSA uses the aerodynamic coefficients of either the long or (near) cubical container configurations shown in Figs. 1 and 2. Not surprisingly, these configurations yield quite different aerodynamic coefficients, which in turns yield differing (free-fall) rotational dynamics [4]. Such sensitivity to shape thus limits the accuracy of DSSA in trajectory analyses of other payload shapes, such as that of a (tall) A-22 container or of type-V platforms carrying land vehicles [1]. This study presents the results of a first series of CFD simulations aimed at enlarging the DSSA input database on aerodynamics coefficients, by including ever-more-realistic payload configurations.

Fig. 1 Pallet-container geometry used in the DSSA implementation of [2–4,9]. This shape is similar to the U.S. Army type-V platform.

The payload configuration consists of the platform-container geometry, as illustrated in Fig. 1 but, in an effort to increase realism, now outfitted with a nose bumper on one side and a cargo enclosure running to the end of the platform, herein labeled the flat side; this geometry is presented in Fig. 3a. Throughout this paper, results are presented with respect to the two flow orientations shown in Fig. 3b. These two flow orientations are simulated in order to provide understanding about the effect of aligning the cargo-pallet configuration in the aircraft so that either the nose bumper or flat side would encounter the oncoming flow when extracted from the aircraft. Results include simulations carried out at a relatively low speed of 30 fps, which would characterize the descent rate prevailing during the descent under parachute, and a moderate speed of 100 fps, which approaches a low-speed drop initial velocity. A variety of static pitch angles (or α) are considered, i.e., -180 to 180°. Such a range well-exceeds the angles sustained during descent but are considered to include the effects of flow orientation and for future comparison with the high-speed cases related to ramp tipoff.

Computational Details

All computations are carried out using the SC/Tetra CFD software on a computer cluster consisting of 10 compute nodes; each compute node contains two quad-core 2.6 GHz processors with 12 GB memory and 500 GB disk space, totaling 80 processors in the cluster. SC/Tetra is a finite volume flow solver using the SIMPLEC [12] method and MUSCL [13] differentiation technique for solving the Reynolds-averaged Navier–Stokes equations with second-order accuracy in space and first-order accuracy in time. Options exist to increase the accuracy to third- and second-order, respectively, but those options were not exercised in this work. All results presented herein use the steady-state solver available in SC/Tetra. SC/Tetra

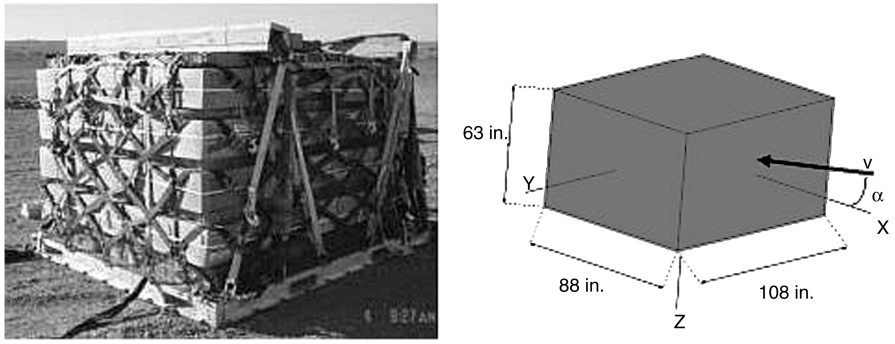

Fig. 2 10K JPADS pallet container (left); idealized version used in DSSA [4]. The direction of the relative wind is represented by the vector V.

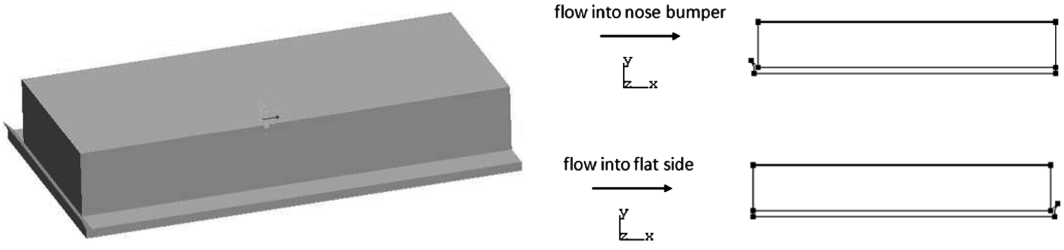

a) Geometry **b) Flow orientations**

Fig. 3 Current-study geometry with an aspect ratio of 0.56.

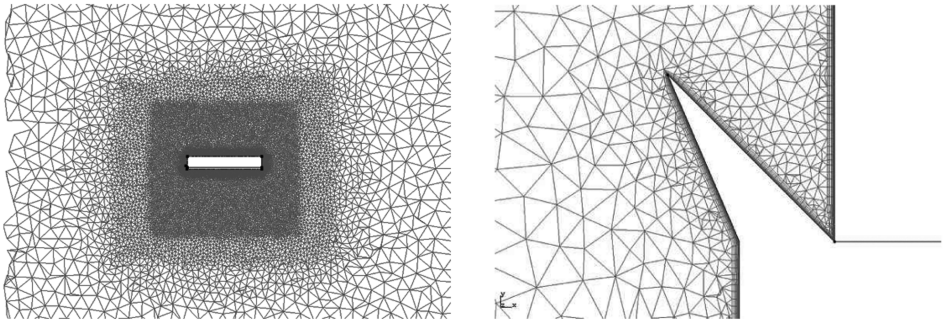

a) Far view **b) Closeup view near nose bumper**

Fig. 4 Computational mesh.

employs an unstructured tetrahedral mesh [14] using prism elements to resolve boundary layers and contains all pre- and postprocessing required for CFD analysis. In this work, the shear stress transport (SST) k-ω turbulence model is used for turbulence closure. The choice of the SST k-ω turbulence model was based on the authors' prior experience with parachute geometries modeling. Because of their bluff shape, such geometries are characterized by separations and larger wakes for which the k-ω model matches experimental data better than the k-ϵ model. Typical run times are on the order of 12–14 h for each 30 fps simulation and near 3 days for each 100 fps simulation. Convergence was determined once the pressure fields became periodic; aerodynamic coefficients presented herein are averaged over this cyclic period.

The pallet and cargo geometry was created in a 3-D modeling program before exporting to stl format for importing into the SC/Tetra preprocessor. The pallet is 192 in. long, 108 in. wide, and 4 in. thick, producing an aspect ratio (width/length) of 0.56. The pallet also contains a typical bumper nose on one end, angled at 45° and measuring 4.39 in. up from the platform and 2.5 in. inside the platform edge. On top of the pallet stands a cargo typically employed in type-V platforms, measuring 191.5 in. long, 81 in. wide and 29 in. tall. This geometry can be seen in Fig. 3. The simulations took advantage of the symmetry in the geometry, so that only half of the model was used in the computations while a free-slip boundary was applied at the symmetry plane at the center running down the length of the geometry along the x axis in the freestream direction. Initial comparisons between the full model and model using the symmetry plane confirmed that using the latter did not significantly affect the results. Both models were simulated at five angles of attack, including −90, 0, 65, 90, and 117°, where drag and lift coefficients agreed within 2%.

A typical computational mesh used for the 30 fps simulations can be seen in Fig. 4a. The three-dimensional domain spanned 15 m away from the center of the geometry in each direction except the symmetry plane and downstream, where it was extended 30 m. These distances were determined by increasing the domain size until the drag, lift, and moment forces did not significantly change with increasing boundary dimension for both the 0 and 90° pitch cases. Between 32 and 34 million elements were used for the 30 fps simulations and between 52 and 61 million elements for the 100 fps simulations. These included tetrahedral elements having an average h ratio between 0.25 and 0.28; likewise, the average surface mesh h ratios were between 0.43 and 0.47. These values indicate the volumetric and surface meshes are of high quality. These meshes were determined by increasing the mesh density in boundary layers and regions of the flow with gradients until the solution results did not appreciably change, similar to the method used for the domain size determination. Figure 4b shows a close-up view of the mesh in the nose-bumper region for the 30 fps case, illustrating the use of prism layers to resolve boundary layers. The inlet plane (left side of Fig. 4a) boundary condition held the velocity constant at 9.144 m/s (30 fps) or 30.48 m/s (100 fps), while the exit plane (right side of Fig. 4a) was held at zero static pressure. The other four sides of the domain (including the symmetry plane) were defined as free-slip boundaries.

Results

Steady-state aerodynamic coefficients are presented first, with pressure coefficient contours to help explain the differences in flow behavior between the two orientations of the geometry with respect to the oncoming flow. Comparisons with other published results follow in order to understand how the current data set augments the available knowledge base.

Figure 5 presents the steady-state lift coefficients for $\alpha = -180$ to 180°, with data supplied at approximately 13° increments, along with previously published data from a CFD study over $-130° \leq \alpha \leq 130°$ on a type-V Low-Velocity Airdrop Delivery System (LVADS) geometry, a 10,000 lb Joint Precision Airdrop Delivery System (10K JPADS) geometry [4], and an experimental study of a 0.56-aspect-ratio flat plate at a Reynolds number range of 3.8×10^4 to 5.7×10^4 over $-10° \leq \alpha \leq 178°$ [8]. The four sets of current data represent the two flow speeds at the two flow orientations that could occur during actual deployment, where the nose bumper or the flat side could encounter the oncoming flow. These four sets follow nearly the same pattern except for small differences mostly confined to two 30° segments in the negative angles of attack approximately between −50 to −80° and between −115 to −145°. This shows that the lift coefficient is generally independent of Reynolds number for the two simulated speeds of 30 and 100 fps. The small differences suggest the lift behavior is not significantly modified due to direction of oncoming flow (into nose bumper or flat side). The current data trends are similar to the previous type-V LVADS CFD data in the positive angles of attack, with more variation with negative α due to the nose bumper, and the flat-plate data are tracked well except in regions of local maxima. The lift behavior of the stubby, cubelike 10K JPADS geometry is not very similar to either of the current flow

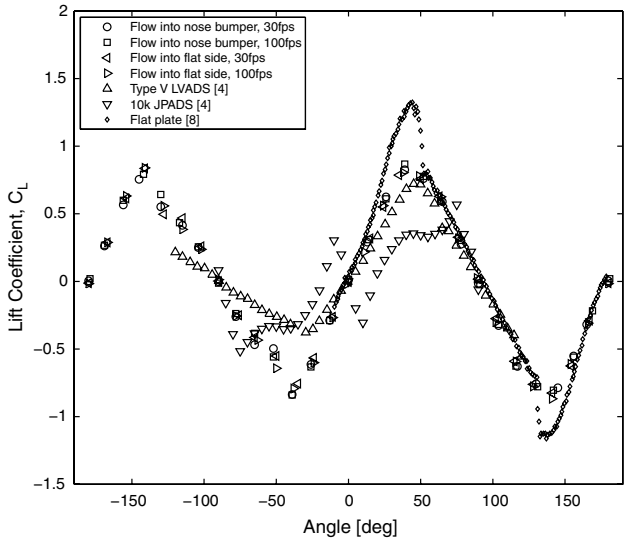

Fig. 5 Lift coefficient vs angle of attack.

Table 1 Lift-curve slopes

α range	$C_{L\alpha}$	R^2
$-145° \le \alpha \le -39°$	−0.015	0.985
$-39° \le \alpha \le 39°$	0.022	0.998
$50° \le \alpha \le 130°$	−0.021	0.991
$141°(-219°) \le \alpha \le -145°$	0.022	0.998

orientations. The maximum lift angles appear to be near 40 and −140° for both orientations, while the minimum lift angles are near 140 and −40°. This high degree of symmetry also suggests lift is not strongly affected by the presence of the nose bumper in lieu of the flat side. These maximum and minimum lift angles lie within 5° of the type-V maximum of 45 and minimum of −35° over the range studied; again, the 10K JPADS maxima do not correspond well to the current data. Desabrais [8] found maximum and minimum lift angles of 44 and 136°, respectively. The current angles lie within 4°, again suggesting only minimal influence of the cargo and nose bumper on lift behavior. Further but subtle differences with thin flat-plate data will be discussed in a later paragraph.

There are four near-linear ranges of lift-curve slope $C_{L\alpha}$, as outlined in Table 1. This table shows the α range, $C_{L\alpha}$, and coefficient of linear regression for the least-squares linear-regression fit over those ranges. These regions occur between −145 and −39°, between −39 and 39°, between 50 and 130°, and between 141 (−219°) and −145°. Of these four ranges, only between −145 and −39° exhibits a slope different than the other ranges (except the expected opposite sign). This is attributed to the two 30° segments noted above which contain small differences between the oncoming flow into the bumper nose and into the flat side of the geometry. The other three ranges exhibit slopes that match the 0.022 value obtained by Torres and Meuller [15] when studying a flat plate at an aspect ratio of 0.5 over $-10° \le \alpha \le 10°$ at a Reynolds number of 7.0×10^4, and these slopes are also similar to the previous flat-plate and type-V LVADS studies included in the figure. This suggests again the lift behavior over the three matching ranges as not being significantly affected by the presence of the cargo on the pallet. The most linear ranges are those with zero lift crossings, judged by the highest coefficient of linear correlation. These ranges are $-39° \le \alpha \le 39°$ and $141°(-219°) \le \alpha \le -145°$, with zero lift crossings at 0 and 180°, respectively. The other two zero lift crossings for $-145° \le \alpha \le -39°$ and $50° \le \alpha \le 130°$ are at −90 and 90°, respectively. These zero lift crossings are exactly where one would expect for a symmetric flat plate and track well with all previous data in the figure, again suggesting the cargo, nose bumper, and flow orientation have minimal effect on the lift behavior.

Figure 6 presents the steady-state drag coefficients for $\alpha = -180$ to 180°, with data supplied approximately every 13°, along with the previous cargo-container and flat-plate studies noted earlier. Again, the 30 fps coefficients track well with the 100 fps results. As expected, and due to the lowest projected area facing the oncoming flow, the minimum drag coefficients occur at 0 and 180° (−180°), 50° outside of the maximum lift angles and 40° inside the minimum lift angles. Because of the similarity in shape, these minimum drag coefficients and angles match very well with the type-V LVADS and flat-plate data, but only the angle of minimum drag (and not the drag magnitude) matches the dissimilar 10k JPADS shape. The authors note that the drag coefficient of the current geometry seems lower than the flat-plate data at zero angle of incidence; however, the flat-plate data at zero incidence were noted as problematic by the author of the original work [8]. Our numerical data with a drag coefficient near 0.14 obtained at a Reynolds number in the millions are actually higher than the standard flat-plate value of 0.002–0.01 quoted in the Reynolds number range 10^4–10^5 as cited by Blevins [16], but smaller than that of a square rod of similar aspect ratio, cited as ≈0.43 by Blevins. Therefore, the authors believe the presented data are accurate. Also as expected, the maximum drag occurs at 90° for both orientations, tracking well with the type-V LVADS and flat-plate data; symmetry at −90° was not found. In fact, the drag behavior between positive and negative angles of attack becomes asymmetric very quickly away from the minimum drag angles, a behavior similar to the type-V LVADS geometry but not to the flat-plate geometry. Unlike the lift behavior, the drag behavior is significantly affected by the cargo and nose bumper, causing the asymmetry seen here. In addition, there are larger differences caused by the flow orientation, most pronounced in the negative angles of attack.

Figure 7 shows pressure coefficient line contours comparing various angles of attack and flow orientations at a Reynolds number of 2.94×10^6. Here, the maximum line-contour value is 1, with a step of 0.1 leading to a minimum line-contour value of −1. The pressure coefficient is defined as the local static pressure minus the freestream static pressure, then divided by the freestream dynamic pressure. Figure 7a shows the pressure coefficient for flow into the nose bumper at 90 and −90° angle of attack, where the positive angle is on the left. This figure shows a higher pressure front and much larger wake at $\alpha = 90°$, explaining the higher pressure drag resulting in the higher drag coefficient in Fig. 6. Figure 7b shows the coefficient of pressure for $\alpha = -65°$, where a significant difference in drag coefficient occurs due to flow orientation. At $\alpha = -65°$, flow into the nose bumper causes more drag than into the flat side, due to the higher pressure in the nose-bumper region. For the flat-side orientation, the nose-bumper region is already submersed in a boundary-layer region with lower pressure, resulting in a lower resistance to flow. At $\alpha = -115°$, the nose-bumper orientation now has the nose bumper submerged in the boundary layer while the flat-side orientation now has the nose bumper exposed out of the boundary layer, causing the higher drag coefficient observed in Fig. 6. These same trends explain the higher drag of the nose-bumper orientation in the $-90° < \alpha < 0°$ region and the opposite behavior observed in the $-90° < \alpha < -180°$ region.

At small angles of incidence we expect good matching between the flat plate and the current geometry in both lift and drag coefficient, since the cargo container looks thin as the result of its small height-to-platform-length aspect ratio. So here we would expect skin drag to be more important, in comparison with the pressure drag effects that would arise from the difference between the front side's stagnation pressure and the back side's wake pressure. Significant differences can be noticed, however, at the larger angles of incidence (i.e., 30 to 50°). As suggested by the sketch of Fig. 8, the container would generate less lift as the angle of incidence causes the upper side of the container to deflect the incoming flow mostly upward, thereby generating a significant downforce; the high angle of incidence would also cause the lower side of the container to create a low-pressure region at its lower edge, thereby creating suction and thus another source of downforce. With regard to drag production, the very presence of the container strapped to the type-V platform may limit the kind of wake collapse seen on very thin plates [8] in that range of incidence angles.

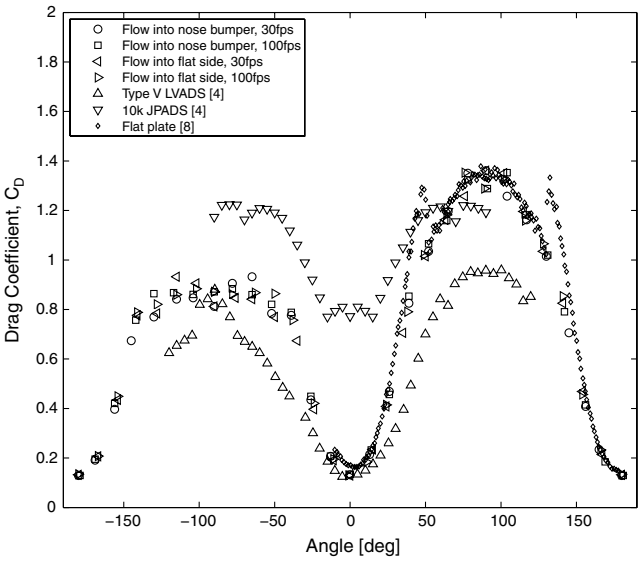

Fig. 6 Drag coefficient vs angle of attack.

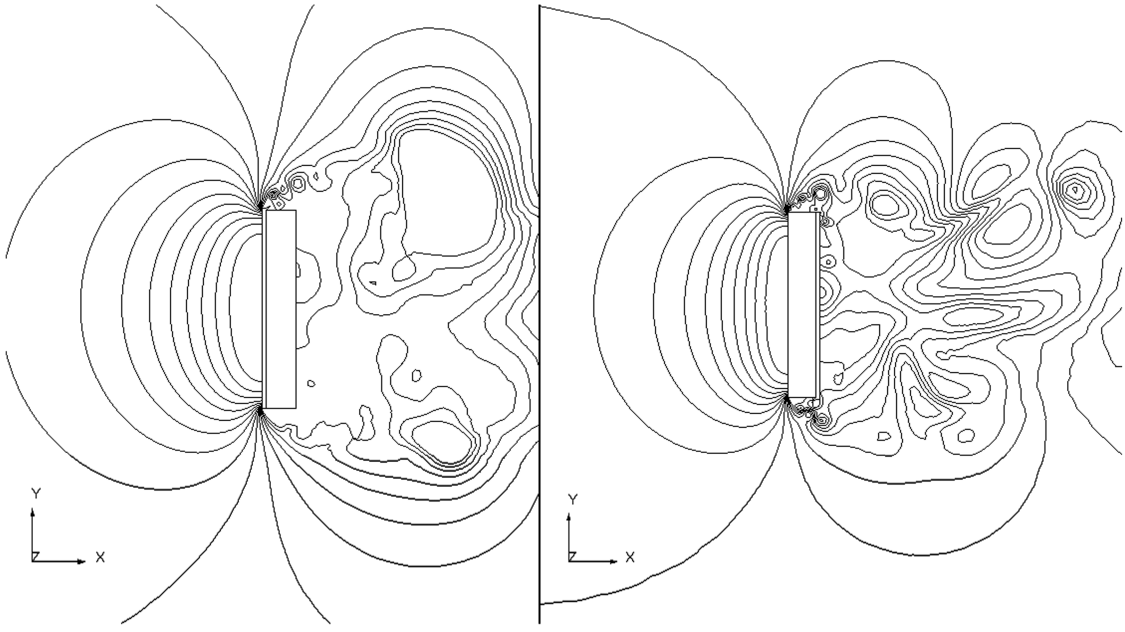

a) α = 90° and α = -90°

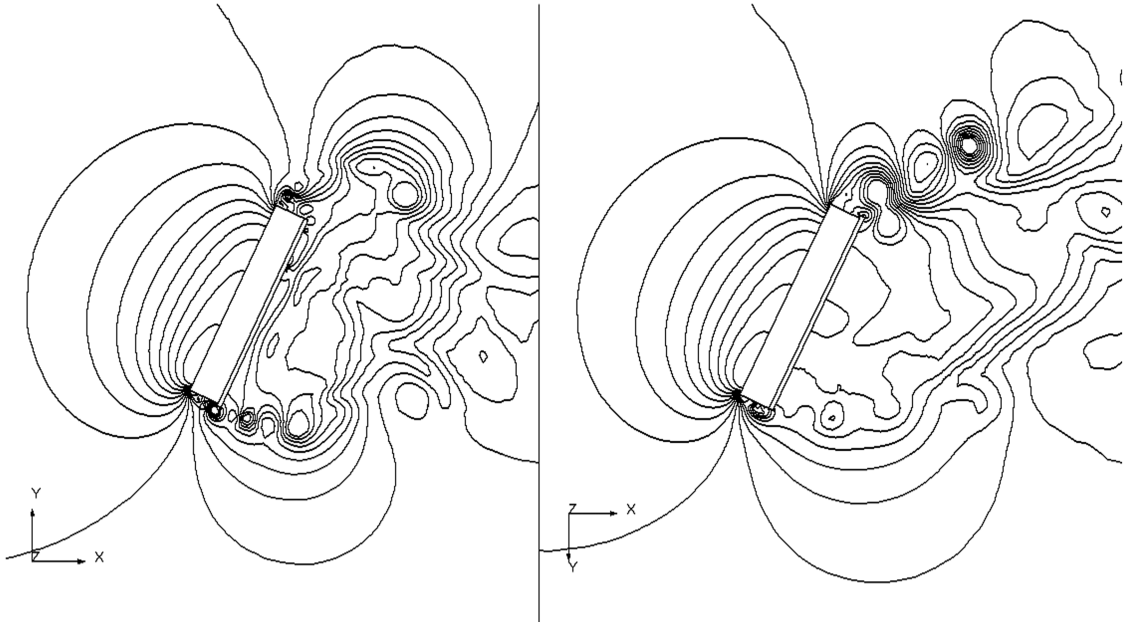

b) α = -65°, °flow into nose bumper orientation on left side

Fig. 7 Line contours of pressure coefficient between angles of attack and flow orientations with flow from left to right; maximum contour value is 1, minimum is −1, with a step of 0.1.

Lifting-line theory can be used to predict drag as a function of lift on finite wings, to yield an equation of the form $C_D = C_{D_0} + K \cdot C_L^2$, where C_{D_0} represents the section drag coefficient of a unit span and the $K \cdot C_L^2$ term represents the drag due to lift. Torres and Mueller [15] found for an aspect ratio of 0.5 that $K = 0.82$ over $-10° \leq \alpha \leq 10°$, while the data taken by Desabrais [8] on a 0.56-aspect-ratio plate show $K = 0.1552$ with $C_{D_0} = 0.140$ over $0° \leq \alpha \leq 43°$. The ranges found to exhibit near-linear behavior between the drag coefficient and the square of the lift coefficient for both flow orientations are shown in Table 2 along with the value of K and C_{D_0}; these are also plotted in Fig. 9 along with the curve determined in Desabrais's study of a flat plate. Comparisons were also made with a second-order polynomial in lift coefficient (as found in many aircraft design textbooks) but yielded poor correlation coefficients. It is interesting that the highest linear correlation (with $R^2 = 0.993$) and positive K corresponds to the angle ranges with a positive lift-curve slope away from the range where drag is asymmetric (from typical flat-plate behavior). In addition, the range with $K = -0.568$ and $R^2 = 0.958$ corresponds to the negative lift-curve slope region for positive angles of attack. There is no good linear correlation for the angle ranges not included in Table 2 (the best fit had $R^2 = 0.325$) in the negative angle-of-attack regions where the drag coefficient behavior is different than the positive angle-of-attack regions due to the effects of the cargo and nose bumper. The flat-plate curve on Fig. 9 from the Desabrais [8] study also has a lower slope magnitude than the present data, while the $K = 0.82$ from Torres and Meuller [15] matches better with the 0.924 found in the positive angle-of-attack range of the current study.

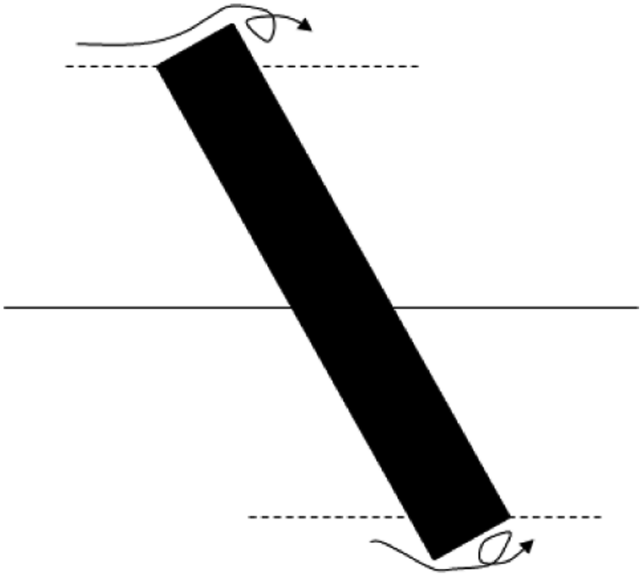

Fig. 8 Sketch of platform at higher incidence angles.

Figure 10 presents the steady-state moment coefficients for $\alpha = -180$ to 180°, with data supplied approximately at every 13°, together with moment data from the 10K JPADS and type-V LVADS CFD. Again, the 30 fps data track very well with the 100 fps results. This figure shows how the flow orientation has a minimal effect on the moment behavior, as the flow into nose-bumper data tracks well with the flow into flat-side data. The moment behavior near zero angle of attack resembles that of the stubbier 10K JPADS geometry, although not with the same slope or peak and trough locations. Only the minimum and maximum values resemble the previous type-V CFD study, although the locations are significantly different. The stable angles, where the moment coefficient curve slope is negative at a zero crossing, are at 0 and 180° for both flow orientations, matching the stubby 10K JPADS result for the data available. This suggests that both flow orientations remain marginally stable during extraction until tipped over by the weight of the cargo or the angle of deployment.

Conclusions

This work simulated the steady-state flows about a pallet and cargo geometry typically employed in parachute airdrop operations. Two flow orientations were studied, with flow entering the nose-bumper side or the flat side where the cargo ends at the length of the pallet. Results show that the lift and moment behaviors are not significantly modified by the difference in flow orientation, and lift-curve slopes matched well with previously published data on pallet and cargo geometries as well as flat plates with similar aspect ratios. Contrary to lift and moment, the drag behavior exhibited significant differences due to the flow orientation. At positive angles of attack, both orientations match trends of flat plates and previous platform and cargo geometries, but at negative angles of attack there were significant asymmetries, which could be attributed to the presence of the nose bumper within or beyond the local boundary layer. In positive angles of attack, the drag coefficient behavior could reasonably be predicted as a linear function of the square of the lift coefficient similar to lifting-line theory. For negative angles of attack, there were very few ranges where linear correlations could relate drag coefficient with the square of lift coefficient. Comparisons of moment coefficient showed that flow orientation has a negligible effect on moment curves, where both flow orientations show stable behavior near 0 and 180° for the steady-state pitch angles simulated herein.

Table 2 Drag coefficient vs lift coefficient squared

α range	K	C_{D_0}	R^2
$-180° \le \alpha \le -141°$, [a] $-39° \le \alpha \le 35°$, $145° \le \alpha \le 180°$	0.934	0.125	0.993
$50° \le \alpha \le 130°$	−0.568	1.365	0.958

[a]The nose-bumper data point at 39° did not fit the linear correlation.

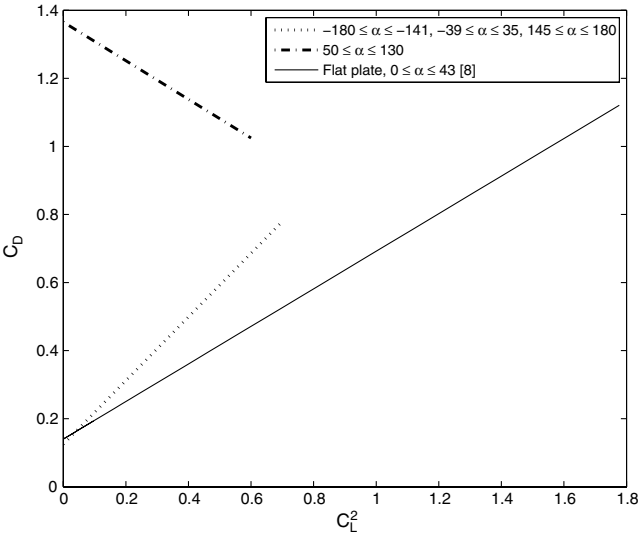

Fig. 9 Drag coefficient vs lift coefficient squared.

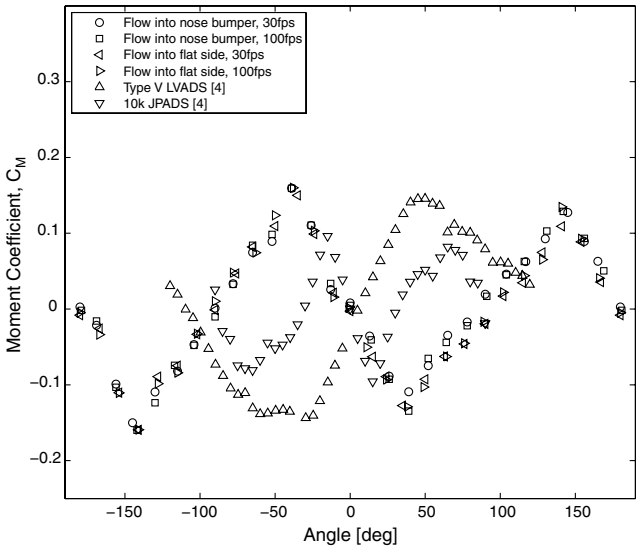

Fig. 10 Moment coefficient vs angle of attack.

Acknowledgments

The authors would like to thank the U.S. Army Natick Soldier Research, Development, and Engineering Center for support of this project through contract W9124R-09-P-1153. The authors would also like to thank Sally Warning for assistance with determining proper mesh refinements.

References

[1] Knacke, T., *Parachute Recovery Systems Design Manual*, Para, Santa Barbara, CA, 1992.

[2] Cuthbert, P., "A Software Simulation of Cargo Drop Tests," AIAA Paper 2003-2132.

[3] Cuthbert, P., and Desabrais, K., "Validation of a Cargo Airdrop Software Simulator," AIAA Paper 2003-2133.

[4] Potvin, J., Charles, R., and Desabrais, K., "Comparative DSSA Study of Payload-Container Dynamics Before, During and After Parachute Inflation," AIAA Paper 2007-2564.

[5] Peterson, C., and Johnson, D., "Reductions in Parachute Drag Due to

Forebody Wake Effects," *Journal of Aircraft*, Vol. 20, No. 1, 1983, pp. 9–42.

[6] Lingard, S., "Wake Effects in Aerodynamics I (Steady)," *H. G. Heinrich Parachute Systems Short Course*, U.S. Army, Yuma Proving Ground, AZ, May 12–16 2008.

[7] Desabrais, K., "The Motion and Aerodynamics of an Airdrop Platform," AIAA Paper 2004-4845.

[8] Desabrais, K., "Aerodynamic Forces on an Airdrop Platform," AIAA Paper 2005-1634.

[9] Cuthbert, P., Conley, G., and Desabrais, K., "A Desktop Application to Simulate Cargo Drop Tests," AIAA Paper 2005-1623.

[10] Moog, R., Smith, N., Corwin, R., and Livezey, W., "Parachute Simulation User's Guide Computer Program UD233A," Martin-Marietta Corp., Denver Aerospace Div., Denver, CO, Feb. 1986.

[11] Machin, R., Stein, J., and Muratore, J., "Overview of the X-38 Prototype Crew Return Vehicle Development and Test Program," AIAA Paper 99-1703.

[12] Patanker, S., *Numerical Heat Transfer and Fluid Flow*, Hemisphere, New York, 1980.

[13] Van Leer, B., "Towards the Ultimate Conservative Difference Scheme 4: A New Approach to Numerical Convection," *Journal of Computational Physics*, Vol. 23, 1977, pp. 267–299.

[14] Rhie, C., and Chow, W. "Numerical Study of the Turbulent Flow Past an Airfoil with Trailing Edge Separation," *AIAA Journal*, Vol. 21, 1983, pp. 1525–1532.
doi:10.2514/3.8284

[15] Torres, G., and Mueller, T., "Aerodynamic Characteristics of Low Aspect Ratio Wings at Low Reynolds Numbers," *Fixed and Flapping Wing Aerodynamics for Micro Air Vehicle Applications*, edited by T. J. Mueller, Progress in Astronautics and Aeronautics, AIAA, Reston, VA, 2001.

[16] Blevins, R., *Applied Fluid Dynamics Handbook*, Krieger, Malabar, FL, 2003.